Check for updates

Preparation and characterization of sulphur and zinc oxide Co-doped graphitic carbon nitride for photo-assisted removal of Safranin-O dye†

Azmat Ali Khan,[a] Abbas Khan, [iD] *[a] Sumayya Khan,[a] Nasrullah Shah,[a] Ajmal Khan,[b] Faheem Nawaz,[c] Asaad Khalid,[d] Afnan Jan[e] and Ahmed Al-Harrasi*[b]

Recently, there has been significant interest in photocatalytic reactions involving graphitic carbon nitride (g-C_3N_4) due to its sp^2-hybridized carbon and nitrogen content and it is an ideal candidate for blending with other materials to enhance performance. Here, we have synthesized and analyzed both doped and undoped g-C_3N_4 nanoparticles. Specifically, we co-doped sulfur (S) into g-C_3N_4, integrated it with ZnO particles, and investigated the photocatalytic potential of these nanocomposites to remove Safranin-O dye. The initial step involved the preparation of pure g-C_3N_4 through calcination of urea. Subsequently, S-g-C_3N_4 was synthesized by calcining a mixture of urea and thiourea with a 3 : 1 ratio. Finally, the ZnO–S-g-C_3N_4 composite was synthesized using the liquid exfoliation technique, with distilled water serving as the exfoliating solvent. These samples were characterized by advanced techniques, including UV-Vis spectroscopy, Fourier-transform infrared spectroscopy (FTIR), X-ray Diffraction (XRD), energy dispersive X-ray (EDX) and scanning electron microscopy (SEM), to assess their crystallinity, morphology, optical properties, and phase purity. Subsequently, these nanocomposites were employed in catalytic and photocatalytic processes to remove the Safranin-O dye (SO). The results highlighted the formation of Z-scheme junction responsible for ZnO–S-g-C_3N_4's significant performance improvement. The comparison of results demonstrated that S-g-C_3N_4 and ZnO–S-g-C_3N_4 composites revealed an effective removal of Safranin-O dye in the presence of UV-light as compared to pure g-C_3N_4, as it was attributed to the phenomenon of improved separation of photogenerated charge carriers as a result of heterojunction formation between S-g-C_3N_4 and ZnO interfaces. In addition to improving photocatalytic performance, this study presents a facile route for producing ZnO–S-g-C_3N_4 composite with superior adsorption capabilities and selectivity.

1. Introduction

The polymeric semiconductor graphitic carbon nitride (g-C_3N_4) has an appealing tri-*s*-triazine ring electrical structure and a medium band gap. It is highly durable against chemical and

[a]Department of Chemistry, Abdul Wali Khan University, Mardan 23200, KP, Pakistan. E-mail: asaster45@gmail.com; abbas80@awkum.edu.pk; muhammadtalhay42@gmail.com; nasrullah@awkum.edu.pk; abbas053@gmail.com; Fax: +92-937-542188; Tel: +92-3408467885

[b]Natural and Medical Sciences Research Center, University of Nizwa, PO Box 33, 616 Birkat Al Mauz, Nizwa, Oman. E-mail: ajmalkhan@unizwa.edu.om; aharrasi@unizwa.edu.om

[c]Department of Environmental Science, Faculty of Life Sciences & Informatics, Balochistan University of Information Technology, Engineering and Management Sciences (BUITMS), Quetta, Pakistan. E-mail: faheem.nawaz@buitms.edu.pk

[d]Substance Abuse and Toxicology Research Center, Jazan University, PO Box: 114, Jazan 45142, Saudi Arabia. E-mail: akahmed@jazanu.edu.sa

[e]Department of Biochemistry, Faculty of Medicine, Umm Al-Qura University, Makkah, Kingdom of Saudi Arabia. E-mail: Amjan@uqu.edu.sa

† Electronic supplementary information (ESI) available. See DOI: https://doi.org/10.1039/d3ra07247a

heat impacts. When the conduction and valence band levels are exactly in balance, photogenerated electron–hole pairs can be separated.[1,2] Due to the polymeric nature and weak van der Waals interaction between adjoining layers, large interlayer spacing like those in graphite is observed, aiding in intercalation with superior physicochemical features.[3] For years, the work of M. Humayun, W. Pi, Y. Yuan *et al.*,[4] has sparked considerable interest in photocatalysis utilizing semiconductors. Recently, metal oxide semiconductors with a wide band gap have been developed, such as TiO_2,[5,6] ZnO,[7] and NiO,[8,9] have been utilized to destroy organic contaminants through photodegradation. Due to its low cost, chemical stability, and non-toxic makeup, polymeric photocatalyst g-C_3N_4 has gained recognition on a global scale.

Numerous modification techniques have been developed over the years to increase the applicability of g-C_3N_4.[10] Hetero-atom doping is an effective way to alter g-C_3N_4's electronic configuration and increase its density of surface charges, leading to notable changes in its properties and applications.[11] Numerous investigations have revealed that, compared to

pristine g-C$_3$N$_4$, doped g-C$_3$N$_4$ demonstrates a more desired energy band structure, higher solar light usage, increased photocarrier separation efficiency, and improved photo-activity.[12] The features of the g-C$_3$N$_4$ matrix, such as dye adsorption and light absorption, can be enhanced by doping it with other inorganic, organic metals or compounds.[13] Among various elements, sulphur (S) doping on g-C$_3$N$_4$ alters the reaction kinetics for transferring photogenerated charge carriers to lower the band gap energy, which increases solar-energy absorption.[14] The g-C$_3$N$_4$ behaves like a conductor as a result of S-doping. The non-uniform distribution of S-over g-C$_3$N$_4$ collects excited electrons, whereas undoped portions act as a photo anode. The entire setting encourages charge separation and higher photocatalytic activity. S-doping causes significant changes in the electrical structure of g-C$_3$N$_4$, narrowing the band gap and converting the material into a conductor, which are particularly noticeable.[15] The length between the S–C bond (1.75 A) is longer than that of the original C–N bond (1.35 A) in terms of sulfur doping chemistry.

Additionally, due to the S and N bonds' differing electronegativity, the band gap of the S-g-C$_3$N$_4$ sheet is 0.20 eV, which is substantially less than the pristine g-C$_3$N$_4$ sheet's band gap of 2.70 eV. This could enable more efficient charge transfer.[16] Due to its resemblance to graphene, g-C$_3$N$_4$ has received much attention in recent studies.[17] It has abundant uses in gas sensors, solar cells, and energy conversion.[18] Polycondensation of common monomers is a typical synthetic method for producing g-C$_3$N$_4$.[19] It possesses fascinating properties such as excellent thermal stability and a high in-plane nitrogen concentration.[20] The composition and physical characteristics of carbon nitrides can be changed by adding heteroatoms, which also engineer the molecular orbital shape and position necessary to improve the material's reactivity and selectivity. By charge transfer complexation or interaction with semiconductor materials, this then aids in creating composites with a high electron density system inside the catalyst.[21]

Water splitting has been extensively researched using g-C$_3$N$_4$ [22] and the removal of organic pollutants in the presence of visible light irradiation[23] due to its low band gap energy range of 2.7–2.9 eV.[24] Nevertheless, it cannot be used in photocatalysis because of its low precise surface area, quick recombination of photogenerated e$^-$–h$^+$ couples, poor adsorption, and poor dispersion.[23] Numerous methods have been researched to modify g-C$_3$N$_4$ in order to increase its photooxidation capacities to get rid of these drawbacks, including customizing the morphologies,[25] doping with metal and non-metal ions,[26] as well as enhancing pore development to increase surface area and adsorption sites.[27] The synthesis of mesoporous g-C$_3$N$_4$ is also an effective approach for improving the catalytic activity of g-C$_3$N$_4$.[28,29] Additionally, the photocatalytic activity can be enhanced by combining g-C$_3$N$_4$ with other semiconductors, preventing charge carrier recombination caused by visible light. Several g-C$_3$N$_4$ based composites, such as TiO$_2$/g-C$_3$N$_4$,[30] ZnO/g-C$_3$N$_4$,[7] Bi$_2$WO$_6$/g-C$_3$N$_4$,[31] and Ag/g-C$_3$N$_4$,[32] have been reported to have good photocatalytic activity.

In this context, the synergetic effects of graphitic carbon nitride (g-C$_3$N$_4$) doped with sulphur and zinc oxide offer a promising opportunity. Incorporating sulphur and zinc oxide into g-C$_3$N$_4$ forms a novel nanocomposite with potential applications in electroflocculation for wastewater treatment. Although, electroflocculation has shown promise as an alternative approach for pollutant removal, it faces limitations that hinder its widespread adoption. One major limitation of conventional electroflocculation methods is the high energy requirement, which leads to increased operational costs and limits its feasibility for large-scale wastewater treatment.[33] Additionally, the removal efficiency of electroflocculation can be limited, particularly for contaminants that are difficult to flocculate and sediment. These challenges emphasize the need for innovative materials and approaches to enhance the efficiency and effectiveness of electroflocculation for advanced wastewater treatment.

Our current study delved into the fascinating realm of co-doping of sulphur and ZnO with g-C$_3$N$_4$. By incorporating sulphur and zinc oxide into the structure of g-C$_3$N$_4$, we aimed to enhance its performance and expand its range of applications. The doping effects improved photocatalytic activity, enhanced charge carrier mobility, and extended absorption spectrum. This research opens up exciting possibilities for developing advanced materials with improved properties, offering promising prospects for various fields such as renewable energy, environmental remediation, and heterogeneous catalysis.

2. Experimental work

2.1. Chemicals used

The chemicals used in the preparation of g-C$_3$N$_4$, S-g-C$_3$N$_4$, ZnO and ZnO–S-g-C$_3$N$_4$ are Urea, thiourea, ethanol, zinc acetate dihydrate, KOH, ethylene glycol, Safranin-O dye, and distilled water. All these chemicals were of sound purity and used without further treatments.

2.2. Synthesis of g-C$_3$N$_4$

12 grams of urea dissolved in a 1 : 1 ratio in a mixture of ethanol and water. The solution was then heated to 100 °C while being continuously stirred. The white precipitates were obtained after the solvent evaporated completely. Aluminum foil was then placed over it before being moved to a crucible, preferably one made of alumina. These precipitates were then calcined at 550 °C in the muffle furnace for three hours. After that, it was permitted to a comfortable temperature. The pale yellow substance was turned into a powder for further testing. The following is the chemical process.
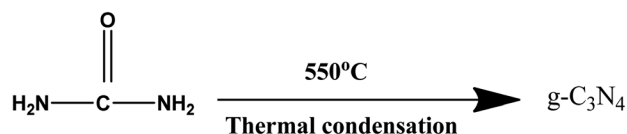
2.3. Synthesis of sulphur doped g-C$_3$N$_4$

Sulphur doped g-C$_3$N$_4$ was synthesized using urea and thiourea as a precursor. Various mixtures of urea and thiourea were

heated at 550 °C for 3 hours with different weight ratios (X : Y), X (urea) and Y (thiourea); such as 3 : 1, 4 : 1, and 5 : 1. Among these mixtures, the S-g-C_3N_4 materials exhibited higher photocatalytic capacity. Notably, the sample with a 3 : 1 composition demonstrated the most active photocatalytic performance. This superiority can be attributed to the higher concentration of doped sulfur in the g-C_3N_4 matrix, which reduced the band gap. Theoretical calculations support these findings, showing that the band gap of sulphur doped g-C_3N_4 material is decreased compared to that of pure g-C_3N_4. Scheme 1 provides a summary of the procedure.

2.4. Synthesis of ZnO nanoparticles

ZnO nanoparticles were prepared using the co-precipitation technique with ethylene glycol as solvent. To fabricate the ZnO nanoparticles, 40 mL of ethylene glycol and 4 grams of zinc acetate dihydrate were added and stirred continuously until a completely transparent solution was achieved. Subsequently, a potassium hydroxide KOH solution was added dropwise to the mixture, maintaining constant stirring. The system's pH was monitored using pH paper, and potassium hydroxide was added until a pH of 9.5 was gradually obtained. After reaching the desired pH, the solvent was completely evaporated, while the suspension was kept in motion by continuous stirring at 210 °C. The resulting dry solid was collected and washed repeatedly with deionized water. These particles were then separated through centrifugation at 4000 rpm for 20 minutes. Following separation, the ZnO nanoparticles were grinded into

fine powder using an agate mortar and subsequently calcined for 4 hours at 600 °C.

2.5. Synthesis of ZnO–S-g-C_3N_4

The ZnO–S-g-C_3N_4 nanocomposite was synthesized by dissolving 0.1 g of S-g-C_3N_4 and 0.06 g of ZnO nanoparticles in separate 30 mL portions of distilled water. Subsequently, the two solutions were mixed while being constantly stirred. After combining the solutions, the suspension was subjected to constant stirring for 30 minutes in a darkened environment with no light to achieve adsorption equilibrium. The resulting material was then dried in an oven. Scheme 1 summarizes the procedure.

2.6. Photocatalytic degradation

The degradation/removal of Safranin-O dye (SO) from wastewater was accomplished by using the prepared nanomaterials in catalysis and photocatalysis, with the help of a 15 W UV-light bulb as light source. Additionally, it was covered to stop light from straying and to focus it on the reaction. Different experiments were conducted by adding specific amounts of catalysts (0.1 g) to a 10 ppm solution of SO and stirring constantly. The equilibrium of dye molecules that are adsorbed and desorbed on the surface of nanocomposites was typically verified by swirling the dye solution in the dark for 20 minutes before subjecting it to UV light irradiation. A predetermined volume of dye solutions was collected and centrifuged at 4000 rpm for 5–10 minutes at regular intervals. Double beam UV-Visible
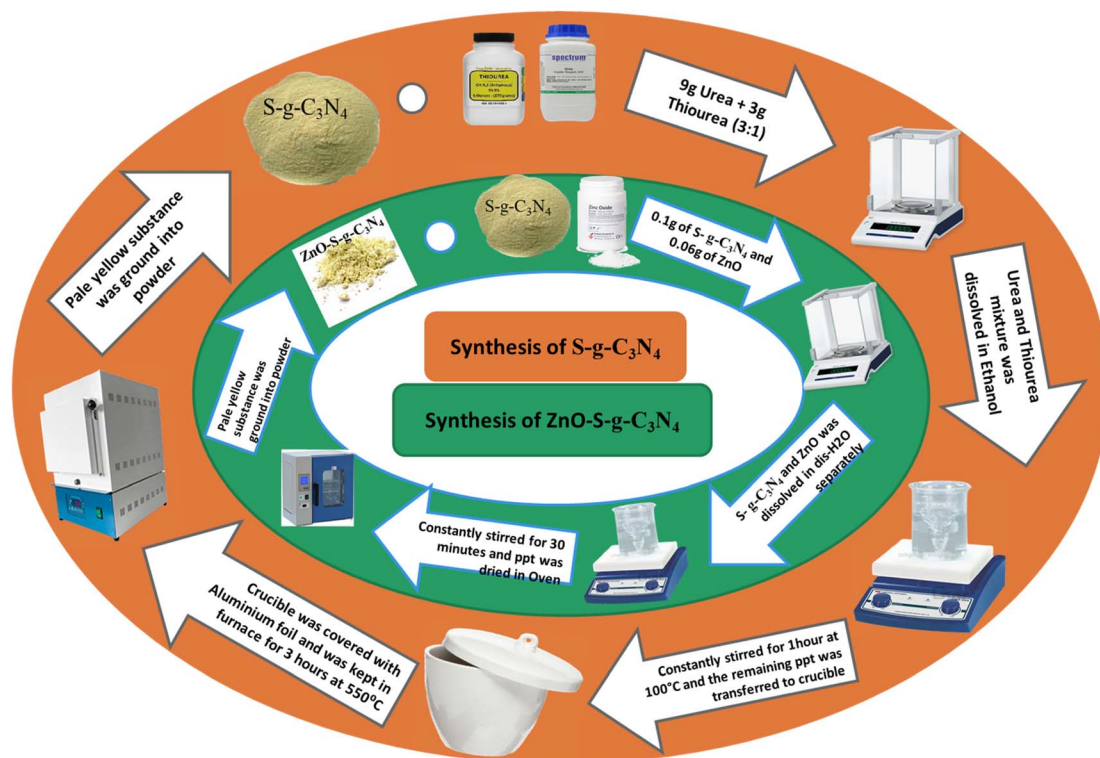
Scheme 1 Schematic representation for the synthesis of S-g-C_3N_4 and ZnO–S-g-C_3N_4.

spectrophotometer (Cary 100 Bio) was used and the dye's absorbance at maximum absorption wavelength was measured to evaluate its concentration during photocatalytic degradation. However, the percentage of removal of the SO dye was assessed as follows:

$$\text{Percent dye degradation} = \left(\frac{C_0 - C_t}{C_0}\right) \times 100 \qquad (1)$$

where "C_0" denotes the initial absorbance and "C_t" denotes the final absorbance at a given time interval.

3. Results and discussion

3.1. UV-Visible absorption spectroscopy

The UV-Visible absorption studies were carried out by dispersing the nanocomposites in ethanol and then analyzed the solution using a UV-Visible Spectrometer Lamda-25 (PerkinElmer). Fig. 1 shows the UV-Visible spectra acquired in the 200–800 nm wavelength range. The energy bandgaps of nanocomposites were determined using the following Tauc plot equation (eqn (2)):

$$(\alpha h \nu)^{\gamma} = A(h\nu - E_g) \qquad (2)$$

where "α" denotes the absorption coefficient, "h" denotes Planck's constant, "ν" denotes the frequency of photons, "A" signify the constant of proportionality, "E_g" symbolize the band gap energy, "γ" indicate the electronic transition whose values can be taken as 2, 1/2, 2/3, or 1/3, depends on transition type.[34] The Tauc's plots for the g-C_3N_4, ZnO, S-g-C_3N_4 and ZnO–S-g-C_3N_4 nanomaterials are indicated in Fig. 2. When $(\alpha h\nu)^2$ was plotted *versus* $(h\nu)$, straight lines demonstrated that directly permitted transitions cause the absorption edges. The optical bandgap (E_g) is represented by the straight-line intercept.

The absorption characteristics of the synthesized materials were identified using UV-Visible spectroscopy. The UV-Visible spectrum of pure g-C_3N_4 exhibits an absorption pattern of
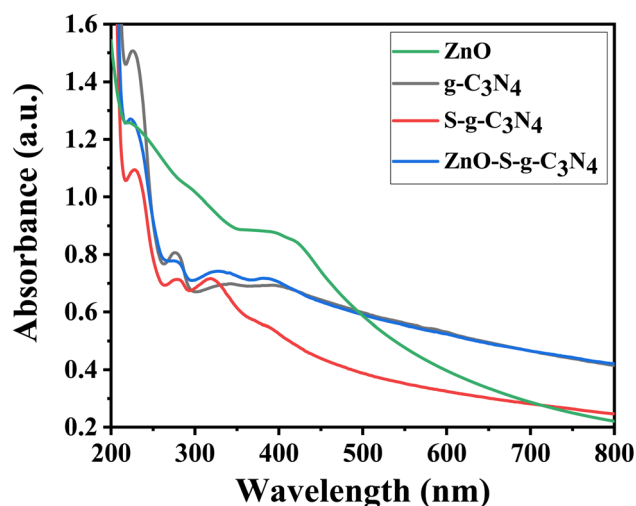

Fig. 1 UV-Visible results of ZnO, g-C_3N_4, S-g-C_3N_4 and ZnO–S-g-C_3N_4 nanocomposite.
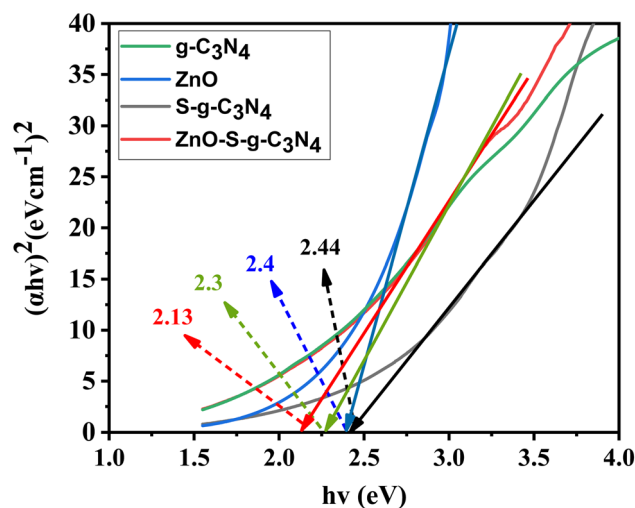

Fig. 2 Bandgap energy results of g-C_3N_4, ZnO, S-g-C_3N_4 and ZnO–S-g-C_3N_4 nanocomposite.

typically semiconductors, spanning the range from 200 to 450 nm. This spectrum results from charge transfer processes, specifically the transition from the populated valence band of nitrogen atoms (2p orbitals) to the conduction band of carbon atoms (2p orbitals) in carbon nitride.[35] Fig. 1 shows the UV-Vis absorption spectra of the prepared samples, including ZnO, g-C_3N_4, S-g-C_3N_4, and ZnO–S-g-C_3N_4. Notably, a prominent absorption band appears in the range of 300–350 nm. This band is associated with electronic transitions in aromatic 1,3,5-triazine compounds, which aligns with the absorption characteristics of this type of transition. These results corroborate the presence of structures based on *s*-triazine rings, supporting the conclusions drawn from the EDX and FTIR analyses. In Fig. 1, the UV-Visible spectroscopy data for ZnO nanoparticles reveal two absorption peaks at wavelengths of 267 nm and 380 nm. These dual peaks are attributed to the elongated shape of the nanoparticles.[36] The peak at 380 nm corresponds to the intrinsic band gap absorption of ZnO, arising from electron transitions between the valence band and the conduction band ($O_2p \rightarrow Zn_3d$). The broad nature of this peak indicates that the particles are on a nanoscale and possess a narrow particle size distribution.[37]

Tauc plots were utilized to determine the consistent energy bandgap of the provided materials using UV-Visible absorption spectra, as shown in Fig. 2. The bandgap energy of ZnO was determined to be 2.4 eV. This accurately characterizes ZnO as a semiconductor material with excellent photoelectric properties in the ultraviolet range but limited reactivity to visible light.[38,39] The absorption edge of g-C_3N_4 is 300–350 nm, which corresponds to the direct bandgap of 2.3 eV. Likewise, the bandgap energy of S-g-C_3N_4 ($E_g = 2.44$ eV) is given more instinctively in Fig. 2.[40] It is attributed to the bandgap alignment resulting from the coupling of semiconductor materials. This indicates that the composite photocatalyst exhibits enhanced response to visible light, which significantly enhances its performance. The bandgap energy of ZnO–S-g-C_3N_4 is

approximately 2.13 eV (Fig. 2). It was observed that a slight increase in the bandgap occurred upon doping sulfur into graphitic carbon nitride. This could be attributed to the smaller atomic radius of sulfur atoms compared to carbon and nitrogen atoms, which may introduce energy levels into the bandgap. These new levels act as traps for electrons, making it more difficult for them to move through the material. As a result, the bandgap increases.[40]. The increased bandgap makes the material more suitable for photocatalytic applications, as it can absorb high energy photons. Similarly, doping sulfur can also improve the charge separation and transfer efficiency, thereby enhancing the photocatalytic activity of the resulting ZnO–S-g-C_3N_4 composite. The observed variations in the overall behavior of ZnO–S-g-C_3N_4 are promising from an application point of views.

3.2. XRD analysis

The X-ray diffraction (XRD) technique is a powerful tool for examining a compound's structure, crystallite size, phase information, and the presence of contaminants within the matrix.[41] In our study, XRD was instrumental in understanding how doping influenced changes in phase morphology and crystal size in the generated nanomaterials.

As illustrated in Fig. 3, the XRD patterns reveal the crystalline nature of the prepared (a) g-C_3N_4, (b) ZnO, (c) S-g-C_3N_4, and (d) ZnO–S-g-C_3N_4 nanocomposites. The XRD pattern of g-C_3N_4 exhibits diffraction peaks at approximately 27.2°, corresponding to the (002) plane of hexagonal g-C_3N_4 geometry.[42] All the synthesized samples exhibit two distinct XRD peaks, (100) and (002) planes, with 2θ angles of approximately 13.1° and 27.2°, respectively, indicative of the typical g-C_3N_4 structure. The smaller intense peak observed at 13.1° is associated with the (100) plane, likely related to the in-plane structural packing motif of g-C_3N_4, such as the distance between nitride pores. Upon the addition of ZnO, the intensity of this smaller peak decreased, suggesting a significant interaction between the g-

C_3N_4 host and the newly introduced ZnO. This interaction influenced the nitride pore structure and altered the hole-to-hole distance.[7] The peak at a higher angle (002) is attributed to the periodic facial stacking of motifs found in conjugated aromatic systems, highlighting the distinctive graphitic structure of g-C_3N_4. In the case of ZnO–S-g-C_3N_4 (Fig. 3(b)), distinct diffraction peaks at 2θ values of 31.23, 33.89, 35.63, 46.88, 55.88, 67.09, 62.28, and 67.36 are observed. These peaks correspond to the hexagonal-structured wurtzite ZnO, confirming that the heterostructures are composed of both g-C_3N_4 and ZnO phases, respectively.[43]

Additionally, the average crystallite size (D_p) calculated, shown in Table S1† from the diffraction peaks using Scherrer's equation.

3.3. FTIR analysis

In order to study chemical bonding and functional groups in molecules, FT-IR analysis is a crucial technique. The FTIR analysis of the produced nanocomposites employed an FT-IR spectrometer from PerkinElmer's series 100 with a resolution of 5 cm^{-1} and a wavenumber range of 4000–400 cm^{-1}. FT-IR results are displayed in Fig. 4(a) and (b). Fig. 4(a) shows that a peak around 1641 cm^{-1} corresponds to the stretching vibration band of C=N. While the stretching vibrations for rings of C–N bonds are clearly apparent at 1533 and 1700 cm^{-1}.[44] Likewise, the peak at 810 cm^{-1} indicates the out-of-plane bending mode of heptazine rings.[45–47] Another peak in the range of 2354 cm^{-1} may be due to the presence of adsorbed CO_2 from the atmosphere/air.[16] The peak of sulphur was not seen in the spectra of S-g-C_3N_4 due to its insignificant existence Fig. 4(a). The stretching vibration of the Zn–O bond is attributed to the small peak at 467 cm^{-1} in Fig. 4(a) of the ZnO–S-g-C_3N_4 FT-IR spectrum. The peak near 3743 cm^{-1} is mainly caused by the amine groups and adsorbed water molecules on the surface of g-C_3N_4.[48] Moreover, the band around 3143 cm^{-1} is also ascribed may be due to stretching modes of the OH of adsorbed H_2O.[49] In general, the presence of the identical peaks in the ZnO–S-g-C_3N_4 sample corroborated the compositional assembly, however the peaks intensities decreased slightly.

Fig. 4(b) displays the FTIR spectra of ZnO in the 4000–400 cm^{-1} range. The formation of ZnO nanoparticles is evident from the appearance of peaks at 3324 cm^{-1} and 1632 cm^{-1}, corresponding to the stretching and bending vibrations of O–H groups in water molecules. Additionally, a peak at approximately 564 cm^{-1} indicates the presence of a metal oxide bond (Zn–O).[50] Furthermore, the peak observed at 2120 cm^{-1} can be attributed to the presence of CO_2 molecules in the surrounding air.[51]

3.4. SEM and TEM analysis

SEM images shown in Fig. 5 represent the texture of g-C_3N_4, S-g-C_3N_4, and ZnO–S-g-C_3N_4. SEM micrographs of g-C_3N_4, S-g-C_3N_4, and ZnO–S-g-C_3N_4 are also presented for comparison. It is clear from Fig. 5(a) and (b) that the g-C_3N_4 samples showed aggregated, smooth, slate-like particles made up of lamellar structures. The layered structure of sample S-g-C_3N_4 was verified by
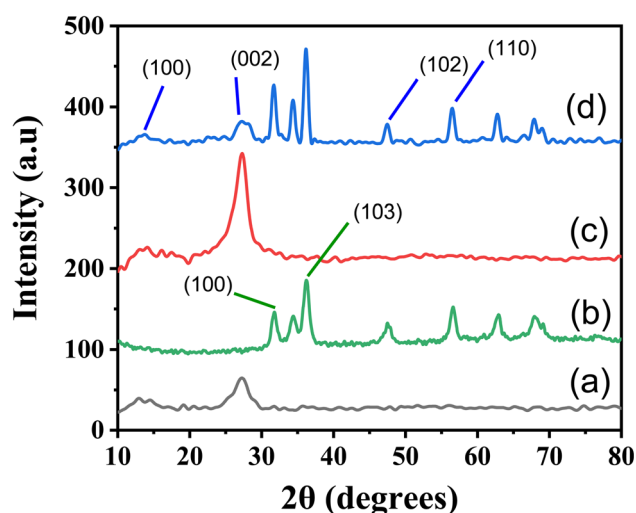

Fig. 3 XRD spectrum of g-C_3N_4 (a), ZnO (b), S-g-C_3N_4 (c) and ZnO–S-g-C_3N_4 (d) nanocomposite.
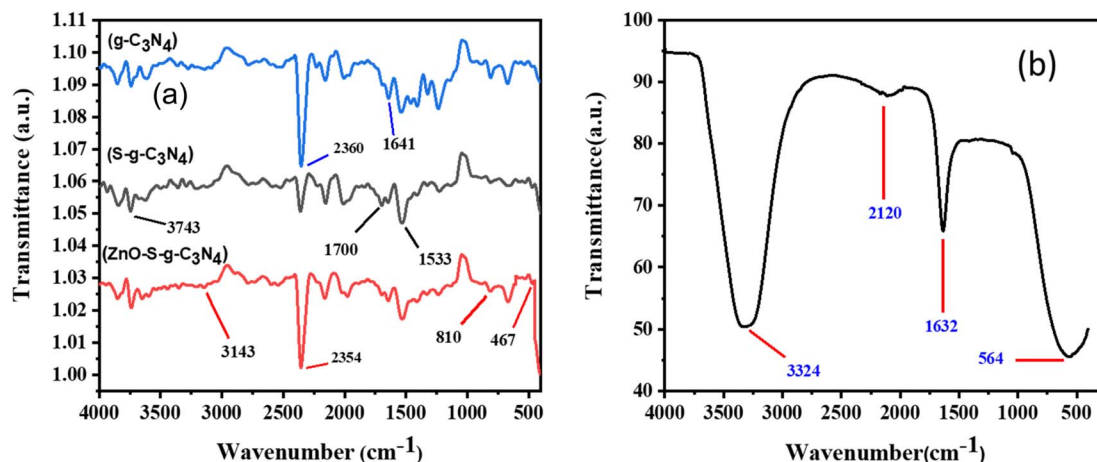
Fig. 4 FTIR spectrum of (a): g-C$_3$N$_4$, S-g-C$_3$N$_4$, ZnO–S-g-C$_3$N$_4$ and (b) ZnO nanocomposite.

microscopic observation. In gas-templating synthesis, layered microstructure is produced by the dense assembly of many irregular nanosheets.[42,52] Interestingly, the pristine g-C$_3$N$_4$ photocatalyst has a non-porous microstructure with tightly connected nanolayers Fig. 5(a) and (b), whereas the S-doped g-C$_3$N$_4$ has a porous microstructure Fig. 5(c) and (d), which is expected to be caused by the emission of ammonia gas during the thermal polymerization of urea and thiourea mixture. The porous, layered structure of the S-doped g-C$_3$N$_4$ photocatalyst has already been hypothesized to be favorable for the development of reactive sites on the catalyst's surface, improving the charge carriers separation and transfer,[53] which is directly related to raising the photocatalyst performance.

Also, it was shown that ZnO–S-g-C$_3$N$_4$ grew into a quench interconnected elongated fiber network after adding ZnO to S-g-C$_3$N$_4$ Fig. 5(e) and (f). A flimsy framework of ZnO–S-g-C$_3$N$_4$ with a higher surface area and porosity was formed when [ZnCO$_3$]$_2$ and [Zn(OH)$_2$]$_3$ interacted with a mixture of urea and thiourea, according to SEM analysis. This occurred most likely as a result of the influence of the gasses generated during the thermal polymerization process.[7] Such heterojunction morphology is praised for increasing the material's surface area, active sites, and corresponding photocatalytic activity.[54,55]

The TEM examination of g-C$_3$N$_4$ reveals that the material has a nanosheet structure, which would be advantageous for the sensing mechanism. The higher surface area could be due to the layered and flaky organization of the g-C$_3$N$_4$.[56] Porous and flocculent structures in the nanomaterials facilitate the departure of charge carriers and thus suppressing recombination (Fig. 6).

3.5. Energy dispersive X-ray spectroscopy (EDX)

Energy dispersive X-ray spectroscopy (EDX) microanalysis was used to check the elemental composition of all the samples. Energy-dispersive X-ray spectroscopy patterns of the g-C$_3$N$_4$, S-g-C$_3$N$_4$, ZnO–S-g-C$_3$N$_4$, and all the hybrid microgels is depicted in Fig. 7, respectively. The EDX result demonstrates the corresponding peaks of the elements. The EDX spectrum of g-C$_3$N$_4$

Fig. 7(a), revealed the existence of carbon (C) and nitrogen (N). According to EDX results of S-g-C$_3$N$_4$ (Fig. 7b) the main elements were C (carbon), N (nitrogen) and S (sulphur). The percentage composition of all the components found in the ZnO–S-g-C$_3$N$_4$ (Fig. 7c) nanocomposite was in the order C > N > O > K > Zn > S. This reveals that C and N have higher content ratios, whereas Zn and S have the lowest concentrations. The identified elements found in the EDX spectrums, confirm the fruitful synthesis of nanomaterials.[57] The mass percent and atomic percent compositions of all the elements are provided in Table S2.†

3.6. Photocatalytic activity

The effectiveness of photocatalysis of the produced samples was evaluated by monitoring the Safranin-O degradation under UV light. Using a light source, the photocatalytic reaction was successfully carried out. 0.1 g of photocatalysts were added to 100 mL of SO solution with 10 ppm of SO. In order to achieve equilibrium between adsorption and desorption, the suspension from the preceding illustration was stirred at room temperature for 30 minutes without light.[58] The liquid was then agitated vigorously while being exposed to ionizing radiation. The solution was periodically extracted to a volume of 4 mL and centrifuged to ensure the solid catalyst was removed. An ultraviolet-visible spectrometer was used to determine the catalyst's dye adsorption capacity and dye degradation efficiency. The amount of already removed dye can be calculated using the formula shown in eqn (3).

$$\text{Efficiency of degradation (\%)} = (C_o - C_t/C_o) \times 100 \qquad (3)$$

where "C_o" signifies initial absorbance and "C_t" signifies the final absorbance, at a given time intervals.

To execute the kinetic studies of the dye degradation process, the specified first-order equation (eqn (4)) was employed for considering the data.[59]
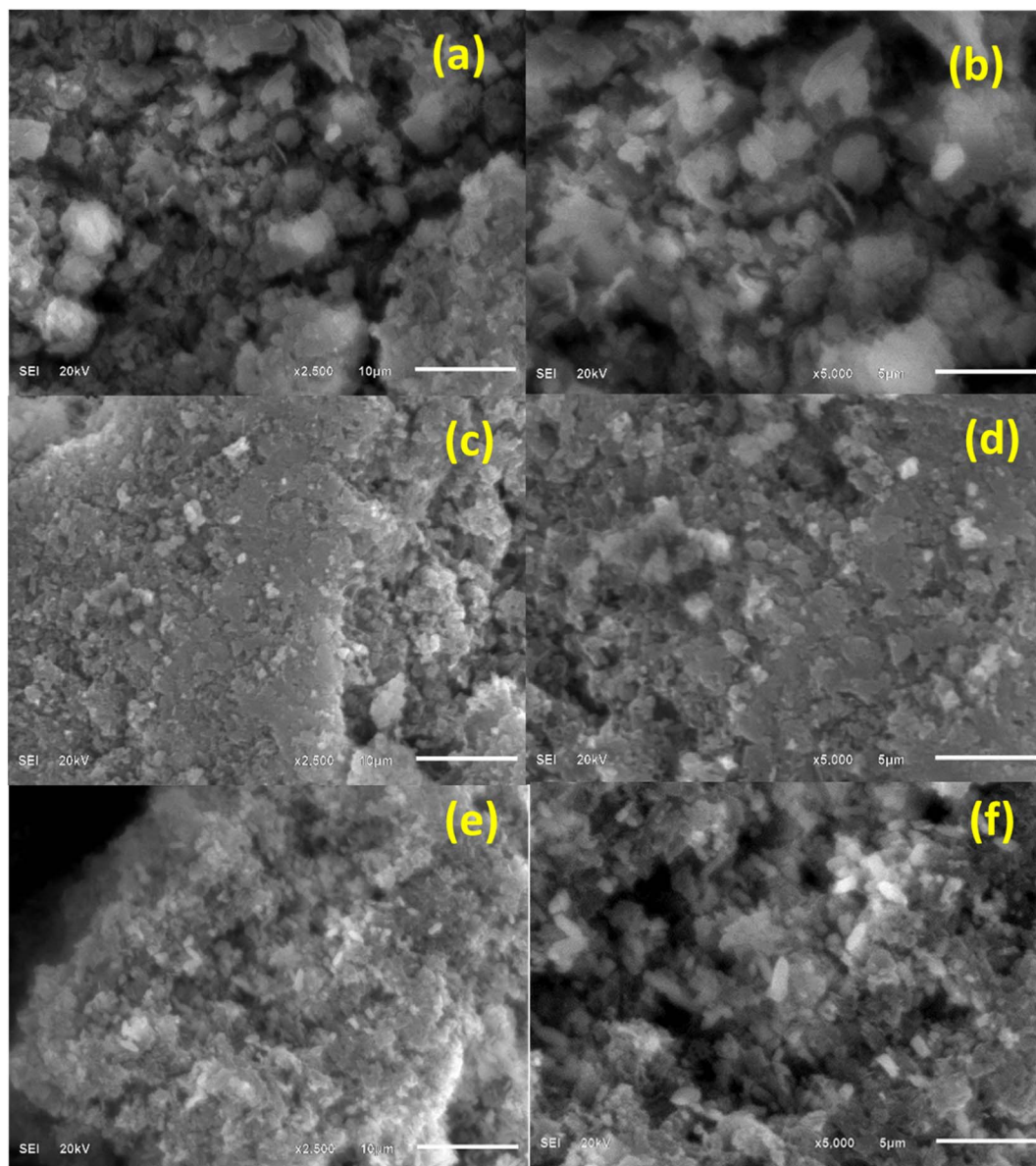
$$\ln(C_t/C_o) = -k_{app} \, t \qquad (4)$$

Fig. 5 SEM images of g-C$_3$N$_4$ (a and b), S-g-C$_3$N$_4$ (c and d) and ZnO−S-g-C$_3$N$_4$ (e and f) nanocomposites.

where "C_o" and "C_t" represent the initial and final concentrations of SO dye at $t = 0$ and $t = t$. Also, the C_o and C_t represent the absorbance at time $t = 0$ and $t = t$. While, k_{app} represents the apparent rate constant of the reaction estimated from the plots slope $\ln(C_t/C_o)$ versus time.[45] In order to compare the photo-assisted dye removal efficiencies of the material with that of their adsorptive dye removal properties, the same experiments were also performed in the absence of light (dark condition) while keeping the rest of the experimental conditions the same.

Fig. S1 and S2† depict the decrease in the absorbance at various time intervals of SO dye in the presence of UV light and dark conditions by synthesized g-C$_3$N$_4$ nanoparticles. Under normal conditions, 10 ppm SO dye solutions were prepared and 0.1 g catalyst dosage was applied; the reaction took up to 360 minutes under UV light. In dark conditions, g-C$_3$N$_4$ removed

less dye than in light conditions. The irradiation suspensions were collected at predefined time intervals. The progression of the degradation was demonstrated by the decreasing SO absorbance over time as displayed in Fig. S1 and S2(a).† As evident from Fig. S1 and S2(b),† the percentage of degradation efficiency increased with time and reached a maximum of 360 and 480 minutes. These results also demonstrate that 20% of the dye was eliminated in the dark in 480 minutes, but in the presence of light, the catalyst removed 69% of SO in 360 minutes. These results indicate that g-C$_3$N$_4$ exhibits higher efficiency in the removal of SO dye in the presence of light compared to its removal in the absence of light. The degradation process of SO dye can be tracked by monitoring changes in the absorbance ratio (C_t/C_0) over time, as illustrated in Fig. S1 and S2(c).† These figures reveal the degradation of SO dye with
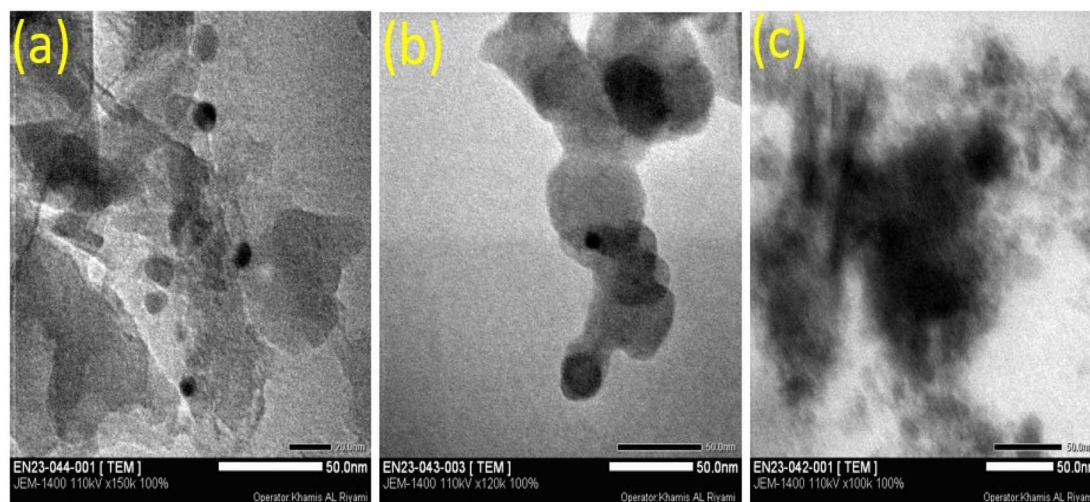
Fig. 6 TEM images of g-C$_3$N$_4$ (a), S-g-C$_3$N$_4$ (b) and ZnO−S-g-C$_3$N$_4$ (c) nanocomposites.

g-C$_3$N$_4$ as a catalyst, where quantitative and qualitative spectral fluctuations occur over time.

Furthermore, Fig. S1 and S2(d)† depict the plot of the pseudo-first-order degradation of SO dye. The data suggest that the reaction follows a pseudo-first-order equation, as indicated by the high values of R^2 ($R^2 = 0.94660$ in the presence of light and $R^2 = 0.97152$ in the absence of light).

The values of the rate constant (K_1), as these numbers for the first-order kinetics, further corroborate this pattern. The values 0.00249, and 0.00041 min^{-1} were used for eliminating SO dye under light and dark conditions, respectively (see Table S3†).

Fig. S3(a) and S4(a)† show the degradation of SO with the S-g-C$_3$N$_4$ catalyst in light and dark, as well as the qualitative and quantitative changes seen with the double beam UV-Visible spectrophotometer. Additionally, the results showed that the SO intensity reduces when the irradiation period is lengthened. This is because of the gradual removal (breakdown) of SO molecules with the passage of time. Furthermore, it is found that the degradation efficiency rises with time and touched a maximum at 270 and 480 minutes, as displayed in Fig. S3(b) and S4(b).† These findings also show that 36.22% of SO was removed in 480 minutes in the absence of light, while in light, the catalyst removed 88.54% of SO in 270 minutes. These results show that the S-g-C$_3$N$_4$ has virtuous efficiency in the degradation of SO dye both in the absence and presence of light, but it works more effectively in the presence of light than in totally
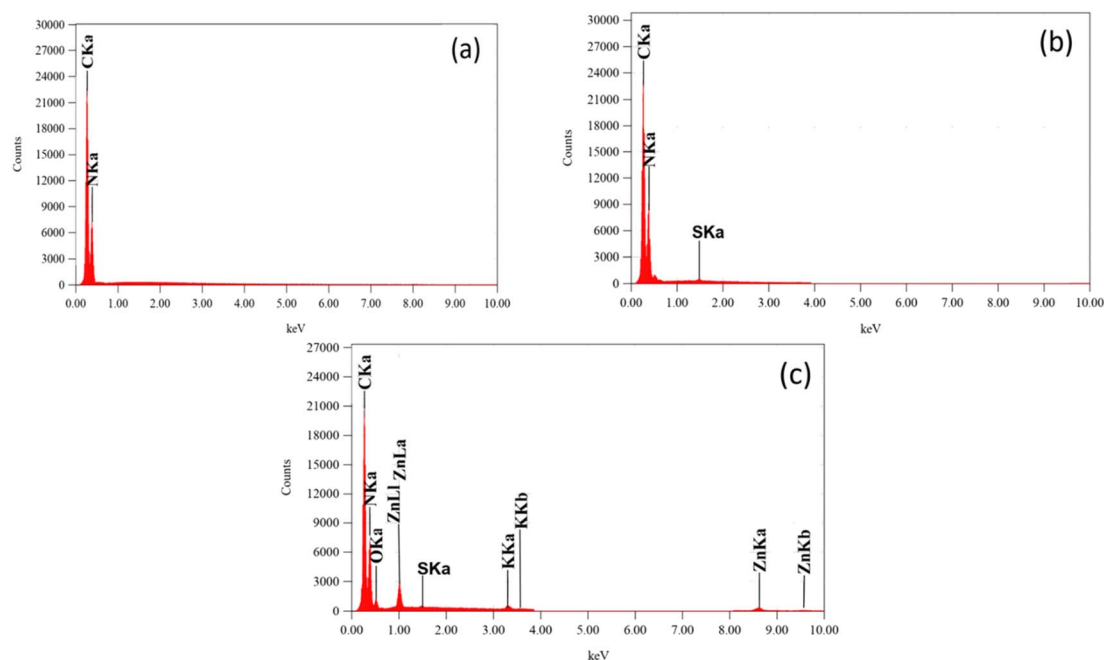

Fig. 7 The elemental composition images of g-C$_3$N$_4$ (a), S-g-C$_3$N$_4$ (b) and ZnO−S-g-C$_3$N$_4$ (c) nanocomposites from EDX.

dark conditions. Furthermore, the plots in Fig. S3(c) and S4(c)† demonstrate the degradation progress in terms of the absorbance ratio (C_t/C_0) *versus* time. These figures illustrate the degradation of SO dye using the S-g-C_3N_4 catalyst, showing both quantitative and qualitative spectral changes over time. Fig. S3(d) and S4(d)† also present the pseudo-first-order relation for the degradation process, confirming that it follows pseudo-first-order kinetics. The high values of R^2 ($R^2 = 0.90922$ in the presence of light and $R^2 = 0.84046$ in the absence of light) support this pattern. Moreover, the rate constant (K_1) values, indicative of the first-order kinetics, were estimated to be 0.00690 in the presence of light and 0.00066 min^{-1} in the absence of light (see Table S3†).

Furthermore, absorbance *versus* wavelength plots of SO dye in light and in the dark for various time periods are shown, using ZnO–S-g-C_3N_4 nanocomposite as a catalyst are illustrated in Fig. 8(a) and 9(a). The graphs clearly specify that the intensity of the absorption peaks of SO lowers from the maximum wavelengths with increasing irradiation period. This is because of effective removal of SO molecules with time. However, after adding ZnO–S-g-C_3N_4; SO demonstrated a sharp peak due to the π–π^* transition and a shoulder peak because of dimeric and polymeric π stacked forms of SO in water.[60] Fig. 8(b) and 9(b) clearly show that the removal efficiency increases with time, as

represented by the plot, at 150 and 480 minutes, respectively, the value reaches its maximum. And that 87% dye elimination happened at 150 minutes in light and 58.64% in dark at 480 minutes, respectively. The plot of absorbance ratio (C_t/C_0) *versus* time is utilized for the removal process, as shown in Fig. 8(c) and 9(c). Fig. 8(d) and 9(d) show the plots of pseudo first-order relations for the SO removal with ZnO–S-g-C_3N_4 catalyst. As confirmed, the degradation data follow a pseudo-first-order equation as shown by the $R^2 = 0.89186$ under light conditions. The first-order rate constant (K_1) value is 0.00989. Similarly, under dark conditions, the $R^2 = 0.75568$, and the first-order rate constant (K_1) is equal to 0.00144 per minute.

A brief comparison of the dye removal performance of the synthesized nanocomposites with a few previously published nanocomposite materials and dyes is shown in Table S3.† The ability of different nanocomposites to remove pollutants might differ depending on the precise pollutant being targeted or the exact nanomaterial being employed. This variability can be attributable to a number of variables, such as variations in light, pH, the concentration of catalysts and pollutants, and differences in chemical structures and reactivity toward pollutants. The dyes compatibility with the nanoparticles may also impact the efficiency of removal. Several surface phenomena occur when a catalyst such as ZnO–S-g-C_3N_4 is used to remove SO dye.
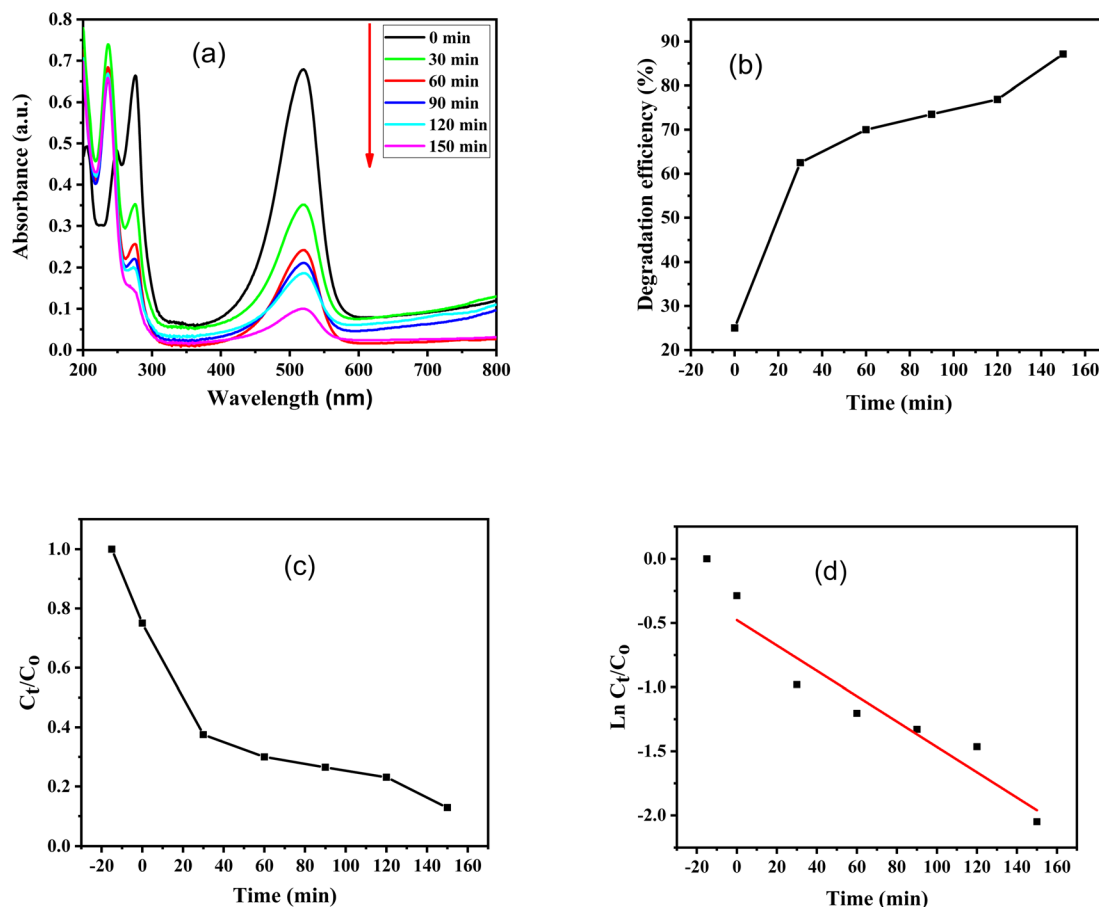

Fig. 8 SO degradation with the aid of 0.1 g ZnO−S-g-C_3N_4 in the presence of light; (a) change in UV-Visible absorbance spectra at different time intervals, (b) degradation efficiency, (c) absorbance ratio (C_t/C_0) *versus* time, (d) plot of pseudo-first-order kinetics of degradation.
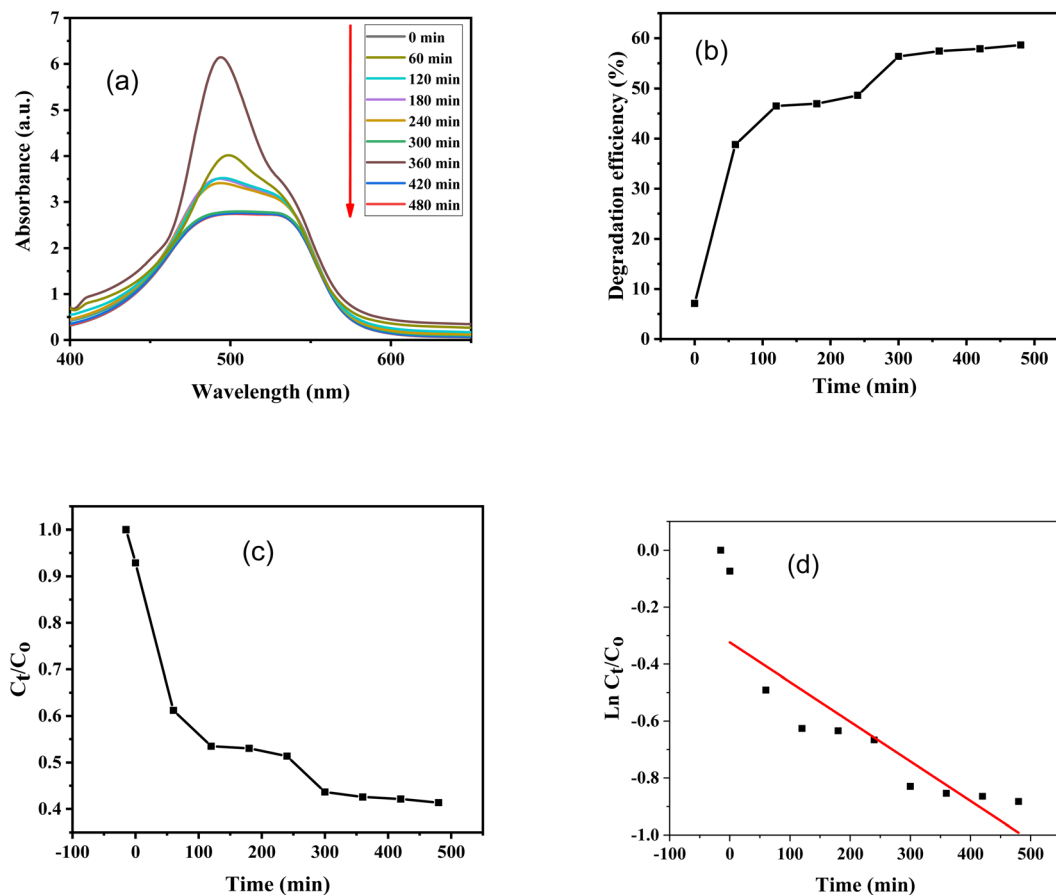
Fig. 9 SO degradation with the aid of 0.1 g ZnO–S-g-C$_3$N$_4$ in the absence of light (dark condition); (a) change in UV-Visible absorbance spectra at different time intervals, (b) degradation efficiency, (c) absorbance ratio (C_t/C_0) *versus* time, (d) plot of pseudo-first-order kinetics of degradation.

The surface of the ZnO–S-g-C$_3$N$_4$ contains active sites where SO molecules may link due to electrostatic interactions, hydrogen bonding, and van der Waals forces. This adsorption process aids in the concentration of dye molecules on the catalyst surface. The photocatalytic action of ZnO is activated after SO molecules are deposited onto the surface of catalyst. When ZnO absorbs photons from light, electron–hole pairs are formed. These photo-induced charge carriers can participate in redox processes, which degrade the SO dye molecules into simpler, less toxic compounds. The S-g-C$_3$N$_4$ can improve the chemical reaction among the dye molecules and the surface of the catalyst. The surface and SO molecules may establish covalent bonds as a result, assisting in their breakdown. So, the adsorption of SO molecules on the surface of the ZnO–S-g-C$_3$N$_4$ catalyst is followed by photocatalytic and possibly chemisorptive activities that helps in the breakdown or elimination of the dye from the polluted water.

It can be concluded that the degradation potential of ZnO–S-g-C$_3$N$_4$ has enhanced as compared to g-C$_3$N$_4$, S-g-C$_3$N$_4$. This could be due to the lower band gap energy of ZnO–S-g-C$_3$N$_4$ nanocomposite, and leads to an enhanced response to light absorption. A decline in photoactivity noticed for g-C$_3$N$_4$ and S-g-C$_3$N$_4$ as compared to ZnO–S-g-C$_3$N$_4$, perhaps because the g-

C$_3$N$_4$ and possesses extra defects that act as the target for electron–hole recombination, slowing down the rate of photo-induced charge transfer. The overall results show that changes in experimental parameters, such as catalyst type, pollutant concentration, catalyst dose, light source, irradiation time, and chemical composition of the dyes, affect the photocatalytic degradation efficiency of the various studies. Additionally, the catalysts' chemical makeup, multiple textures, and morphological characteristics have a significant impact on how effective they are. It's crucial to design core–shell materials that have a suitable balance of hydrophilicity and hydrophobicity.

Finally, it can be concluded that the g-C$_3$N$_4$, S-g-C$_3$N$_4$, ZnO–S-g-C$_3$N$_4$ nanomaterials exhibit significant catalytic activity for the removal of SO dye in light as compared to dark, as it can be seen from their percent removal values provided in Table S3.† However, it is concluded that under alike experimental conditions, SO could be readily degraded by ZnO–S-g-C$_3$N$_4$ compared to g-C$_3$N$_4$ and S-g-C$_3$N$_4$.

3.6.1 Photocatalysis principles and mechanistic mechanisms. Four critical phases make up the majority of the photocatalyst based degradation of organic contaminants process. (1) Pollutant molecules adhere to the catalyst's surface; (2) the catalyst absorbs light; and (3) an electrons–holes pair forms in
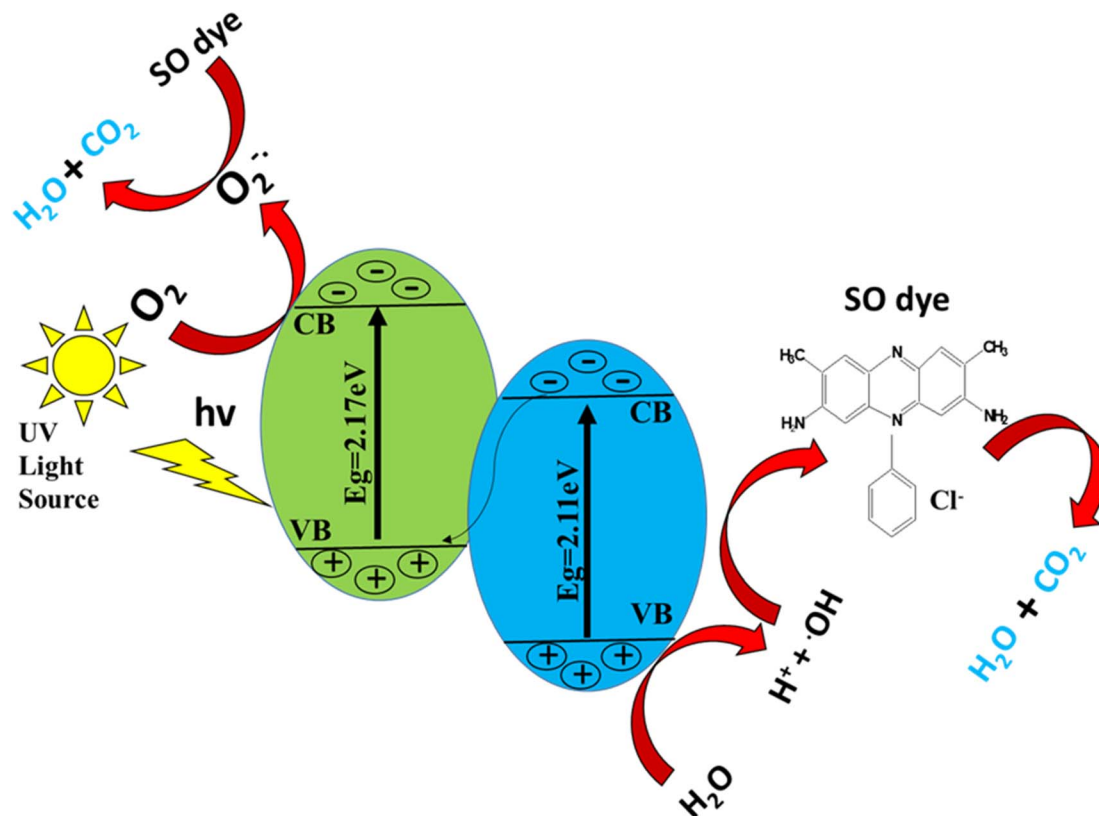
Scheme 2 Schematic diagram for UV-light photocatalytic mechanism showing the generation of oxidative species and degradation of contaminants with the help of a catalyst.

the catalyst's valence and conduction bands. (4) production of superoxide (O^{2-}) and hydroxide (OH.) radical species (5) oxidation of organic contaminants into non-toxic products.

The photocatalytic discoloration of a dye is supposed to be caused by the following mechanism. When a catalyst is exposed to UV light, electrons are moved from the valence band to the conduction band. Consequently, an electron–hole pair is created;[61]
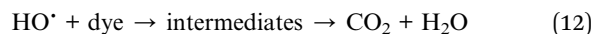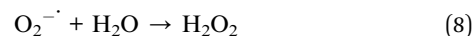
$$\text{Catalyst} + hv \rightarrow e_{cb}^- + h_{vb}^+ \tag{5}$$
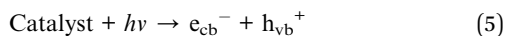
where, e_{cb}^- and h_{vb}^+ are the electrons in the conduction band and the electrons in the valence band, correspondingly. Both of these things can go to the catalyst surface, where they can join other species in a redox reaction.[62] Most of the time, h_{vb}^+ can easily form ˙OH radicals when reacting with surface-bound H_2O, but e_{cb}^- can easily produce superoxide radical anion of oxygen when reacting with O_2.

$$H_2O + h_{vb}^+ \rightarrow \text{˙OH} + H^+ \tag{6}$$

$$O_2 + e_{cb}^- \rightarrow O_2^{-˙} \tag{7}$$
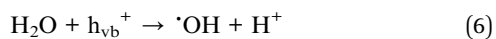
The combination of the electron and the hole created in the first step is prevented by this reaction.

The dye discoloration is caused by the ˙OH and O_2˙ that are created in the manner described above, which can then interact with the dye to form additional species.[63]

$$O_2^{-˙} + H_2O \rightarrow H_2O_2 \tag{8}$$

$$H_2O_2 \rightarrow 2\,\text{˙OH} \tag{9}$$

$$\text{˙OH} + \text{dye} \rightarrow \text{dye}_{ox} \tag{10}$$

$$\text{Dye} + e - cb \rightarrow \text{dye}_{red} \tag{11}$$

$$\text{HO˙} + \text{dye} \rightarrow \text{intermediates} \rightarrow CO_2 + H_2O \tag{12}$$

The powerful oxidizing species known as ˙OH degrades the organic pigment non-selectively into H_2O, CO_2 and inorganic ions.[64,65]

In addition, the oxidation reaction occurs on the VB of ZnO in the ZnO–S-g-C_3N_4 photocatalytic system, while the reduction reaction happens on the CB of S-g-C_3N_4,[66] indicating that the ZnO–S-g-C_3N_4 heterojunction retains its strong redox properties. We also conclude that the heterojunction generated by S-g-C_3N_4 and ZnO is a Z-scheme heterojunction (Scheme 2), also the composite is a photocatalyst with high separation efficiency of photogenerated electron–hole pairs and high redox ability.[46,48,67] A few years back, Kang's group proposed a direct Z-scheme heterojunction photocatalyst based on g-C_3N_4/ZnO in binary

form. Mesoporous ZnO nano-triangles@g-C_3N_4 nanofoils (ZnO-nt@g-C_3N_4) were created using varying g-C_3N_4 concentrations. Under solar light irradiation, the photocatalyst ZnO-nt@g-C_3N_4 (20%) demonstrated 100% degradation of Rh B dye in 60 minutes.[68] Wang *et al.* subsequently presented a Z-scheme mechanism mediated by oxygen defects in exfoliated g-C_3N_4 nanosheets connected to oxygen-defective ZnO (OD-ZnO) nanorods, *i.e.*, CN/OD-ZnO heterojunction with variable wt% of g-C_3N_4.[69] In the case of the GCN-ZnO0.4 sample, the increased surface area can result in decreased recombination of photogenerated charge carriers as well as more active sites during the photocatalytic reaction, which can produce more photogenerated electrons.[70] Scheme 2 illustrates a schematic representation of the mechanisms of oxidative species formation in a photocatalytic investigation. Therefore, in the case of the ZnO–S-g-C_3N_4, both increased surface area and improved light absorption ability can result in superior degradation efficiency toward the SO dye.

4. Conclusion

The g-C_3N_4, was prepared by the calcination of urea, while S-g-C_3N_4 was synthesized by calcination of the mixture of urea and thiourea in a 3:1 ratio. Finally the ZnO–S-g-C_3N_4 nanocomposite was synthesized using the liquid exfoliation technique, and distilled water was used as exfoliating solvent. Numerous characterization techniques such as UV-Visible spectroscopy, FTIR, XRD, EDX, SEM and TEM were used for the as prepared nanomaterials; in order to determine crystallinity, morphology, optical properties, and phase purity. Additionally, the direct-bandgap energy of the nanocomposites was determined, and it agrees strongly with the previously published work. The nanocomposites were employed for catalytic and photocatalytic applications toward Safranin-O dye degradation. According to a comparison of recent findings with those from earlier research, various experimental factors, including the type of catalyst and pollutant, their quantity, the reaction medium's pH, temperature, the quality of the light, and the presence of additional precursors in solution, have a significant impact on the photodegradation of dyes. Overall, it is confirmed that the ZnO–S-g-C_3N_4 and S-g-C_3N_4 nanocomposites have an active catalytic and photocatalytic performance as compared to pure g-C_3N_4, as indicated by their *k*-values. According to the kinetic evaluation, this removal procedure follows a pseudo first-order kinetics. In fact, the suggested approach creates new avenues for the development of effective electrocatalysts for water splitting, which yields hydrogen as a clean energy source. Lastly, we suggest that these materials can be used to degrade the pollutants and pathogens from waste water with high efficiency and stability, also it can be used to enhance the electroflocculation process and contribute to the development of a sustainable approach for advanced wastewater treatment.

Author contributions

All authors have contributed to this study at different stages. Azmat Ali Khan and Abbas Khan: study design, method design,

Conflicts of interest

No potential conflict of interest was reported by the author(s).

Acknowledgements

References

1 S. Kumar, V. R. Battula and K. Kailasam, *Carbon*, 2021, **183**, 332–354.

2 M. A. Qamar, S. Shahid, M. Javed, M. Shariq, M. M. Fadhali, O. Madkhali, S. K. Ali, I. S. Syed, M. Y. Awaji and M. Shakir Khan, *Catalysts*, 2022, **12**, 1388.

3 X. Xiao, J. Wei, Y. Yang, R. Xiong, C. Pan and J. Shi, *ACS Sustainable Chem. Eng.*, 2016, **4**, 3017–3023.

4 M. Humayun, W. Pi, Y. Yuan, L. Shu, J. Cao, A. Khan, Z. Zheng, Q. Fu, Y. Tian and W. Luo, *J. Colloid Interface Sci.*, 2021, **599**, 484–496.

5 M. Verma and A. Haritash, *J. Environ. Chem. Eng.*, 2019, **7**, 102886.

6 M. A. Qamar, M. Javed, S. Shahid, M. Shariq, M. M. Fadhali, S. K. Ali and M. S. Khan, *Heliyon*, 2023, **9**, e12685.

7 D. R. Paul, S. Gautam, P. Panchal, S. P. Nehra, P. Choudhary and A. Sharma, *ACS Omega*, 2020, **5**, 3828–3838.

8 N. R. Vempuluru, C. K. Krishnan, R. Parnapalli, J. Velusamy, S. Marappan, S. Pitchaimuthu, M. Murikinati and S. M. Venkatakrishnan, *Ceram. Int.*, 2021, **47**, 10206–10215.

9 A. BaQais, M. Shariq, E. Almutib, N. Al-Qasmi, R. Azooz, S. K. Ali, K. Hassan and M. Iqbal, *Eur. Phys. J. Plus*, 2023, **138**, 1–9.

10 X. Dong and F. Cheng, *J. Mater. Chem. A*, 2015, **3**, 23642–23652.

11 L. Jiang, X. Yuan, Y. Pan, J. Liang, G. Zeng, Z. Wu and H. Wang, *Appl. Catal., B*, 2017, **217**, 388–406.

12 J. Fu, B. Zhu, C. Jiang, B. Cheng, W. You and J. Yu, *Small*, 2017, **13**, 1603938.

13 M. Humayun, H. Ullah, J. Cao, W. Pi, Y. Yuan, S. Ali, A. A. Tahir, P. Yue, A. Khan and Z. Zheng, *Nano-Micro Lett.*, 2020, **12**, 1–18.

14 A. Hussain, N. Ali, S. Ali, J. Hou, I. Aslam, H. Naeem, M. Boota, M. Ul-Hussan, J. Yin and X. Wang, *Res. Chem. Intermed.*, 2022, **48**, 2857–2870.

15 F. Raziq, M. Humayun, A. Ali, T. Wang, A. Khan, Q. Fu, W. Luo, H. Zeng, Z. Zheng and B. Khan, *Appl. Catal., B*, 2018, **237**, 1082–1090.

16 M. Javed, M. Abid, S. Hussain, D. Shahwar, S. Arshad, N. Ahmad, M. Arif, H. Khan, S. Nadeem and H. Raza, *Dig. J. Nanomater. Biostruct.*, 2020, **15**, 1097–1105.

17 Y. Zheng, Y. Liu, X. Guo, Z. Chen, W. Zhang, Y. Wang, X. Tang, Y. Zhang and Y. Zhao, *J. Mater. Sci. Technol.*, 2020, **41**, 117–126.

18 W. Pi, M. Humayun, Y. Li, Y. Yuan, J. Cao, S. Ali, M. Wang, H. Li, A. Khan and Z. Zheng, *Int. J. Hydrogen Energy*, 2021, **46**, 21912–21923.

19 J. Liu, H. Wang and M. Antonietti, *Chem. Soc. Rev.*, 2016, **45**, 2308–2326.

20 L. Tan, J. Xu, S. Li, D. Li, Y. Dai, B. Kou and Y. Chen, *Materials*, 2017, **10**, 484.

21 G. M. Veith, L. Baggetto, L. A. Adamczyk, B. Guo, S. S. Brown, X.-G. Sun, A. A. Albert, J. R. Humble, C. E. Barnes and M. J. Bojdys, *Chem. Mater.*, 2013, **25**, 503–508.

22 J. Wang, H. Zhao, B. Zhu, S. Larter, S. Cao, J. Yu, M. G. Kibria and J. Hu, *ACS Catal.*, 2021, **11**, 12170–12178.

23 R. Liu, W. Yang, G. He, W. Zheng, M. Li, W. Tao and M. Tian, *ACS Omega*, 2020, **5**, 19615–19624.

24 V. Ragupathi, P. Panigrahi and N. G. Subramaniam, *Optik*, 2020, **202**, 163601.

25 R. Liu, Z. Chen, Y. Yao, Y. Li, W. A. Cheema, D. Wang and S. Zhu, *RSC Adv.*, 2020, **10**, 29408–29418.

26 A. Mittal, B. Mari, S. Sharma, V. Kumari, S. Maken, K. Kumari and N. Kumar, *J. Mater. Sci.: Mater. Electron.*, 2019, **30**, 3186–3207.

27 C. Retamoso, N. Escalona, M. González, L. Barrientos, P. Allende-González, S. Stancovich, R. Serpell, J. Fierro and M. Lopez, *J. Photochem. Photobiol., A*, 2019, **378**, 136–141.

28 A. Hassani, P. Eghbali and Ö. Metin, *Environ. Sci. Pollut. Res.*, 2018, **25**, 32140–32155.

29 A. Hassani, M. Faraji and P. Eghbali, *J. Photochem. Photobiol., A*, 2020, **400**, 112665.

30 I.-H. Tseng, Y.-M. Sung, P.-Y. Chang and C.-Y. Chen, *Polymers*, 2019, **11**, 146.

31 W. Wang, M. Zhang, B. Zhao, L. Liu, R. Han and N. Wang, *Pigm. Resin Technol.*, 2022, **51**, 91–100.

32 D. R. Paul, R. Sharma, P. Panchal, R. Malik, A. Sharma, V. K. Tomer and S. Nehra, *J. Nanosci. Nanotechnol.*, 2019, **19**, 5241–5248.

33 X. Sun, X. Wang, Y. Liu, Y. Lian, L. Meng and Z. Su, *J. Water Process Eng.*, 2022, **47**, 102747.

34 M. Benedet, G. A. Rizzi, A. Gasparotto, O. I. Lebedev, L. Girardi, C. Maccato and D. Barreca, *Chem. Eng. J.*, 2022, **448**, 137645.

35 A. Kumar, P. Kumar, C. Joshi, M. Manchanda, R. Boukherroub and S. L. Jain, *Nanomaterials*, 2016, **6**, 59.

36 R. Augustine, E. A. Dominic, I. Reju, B. Kaimal, N. Kalarikkal and S. Thomas, *RSC Adv.*, 2014, **4**, 24777–24785.

37 H. Karimi-Maleh, K. Ahanjan, M. Taghavi and M. Ghaemy, *Anal. Methods*, 2016, **8**, 1780–1788.

38 M. M. Obeid, H. R. Jappor, K. Al-Marzoki, I. A. Al-Hydary, S. J. Edrees and M. M. Shukur, *RSC Adv.*, 2019, **9**, 33207–33221.

39 N. Aslan, *Türk Doğa ve Fen Dergisi*, 2022, **11**, 95–101.

40 H. Starukh and P. Praus, *Catalysts*, 2020, **10**, 1119.

41 S. Muhammad, A. Ali, S. Zahoor, X. Xinghua, J. Shah, M. Hamza, M. Kashif, S. Khan, B. K. A. Khel and A. Iqbal, *Acta Sci. Appl. Phys.*, 2023, **3**, 33–48.

42 S. Shoran, A. Sharma and S. Chaudhary, *Environ. Sci. Pollut. Res.*, 2023, 1–15.

43 H. Qin, Y. Zuo, J. Jin, W. Wang, Y. Xu, L. Cui and H. Dang, *RSC Adv.*, 2019, **9**, 24483–24488.

44 X. Yang, B. Tang, T. Wu and X. Cao, *J. Mater. Civ. Eng.*, 2019, **31**, 04019141.

45 C. Zhang, Z. Ouyang, Y. Yang, X. Long, L. Qin, W. Wang, Y. Zhou, D. Qin, F. Qin and C. Lai, *Chem. Eng. J.*, 2022, **448**, 137370.

46 L. Yan, H. Gao and Y. Chen, *ACS Appl. Nano Mater.*, 2021, **4**, 7746–7757.

47 S. Benedoue, M. Benedet, A. Gasparotto, N. Gauquelin, A. Orekhov, J. Verbeeck, R. Seraglia, G. Pagot, G. A. Rizzi and V. Balzano, *Nanomaterials*, 2023, **13**, 1035.

48 X. Guo, J. Duan, C. Li, Z. Zhang and W. Wang, *J. Mater. Sci.*, 2020, **55**, 2018–2031.

49 M. Yaseen, A. Khan, M. Humayun, S. Farooq, N. Shah, S. Bibi, Z. A. Khattak, A. U. Rehman, S. Ahmad and S. M. Ahmad, *Macromol. Mater. Eng.*, 2023, 2200695.

50 D. Tamilselvi, N. Velmani and K. Rathidevi, *Egypt. J. Chem.*, 2019, **62**, 785–795.

51 Z.-Y. Zhao, M.-H. Wang and H.-P. Zhang, *J. Mater. Sci.: Mater. Electron.*, 2016, **27**, 1777–1782.

52 M. Benedet, A. Gallo, C. Maccato, G. A. Rizzi, D. Barreca, O. I. Lebedev, E. Modin, R. McGlynn, D. Mariotti and A. Gasparotto, *ACS Appl. Mater. Interfaces*, 2023, **15**, 47368–47380.

53 V. Mariyappan, N. Karuppusamy, T.-W. Chen, S.-M. Chen, J. Jesuraj, M. Akilarasan, B.-S. Lou and J. Yu, *Process Saf. Environ. Prot.*, 2023, **169**, 776–787.

54 M. Javed, M. A. Qamar, S. Shahid, H. O. Alsaab and S. Asif, *RSC Adv.*, 2021, **11**, 37254–37267.

55 H. Li, Y. Wu, Z. Xu and Y. Wang, *Chem. Eng. J.*, 2023, 147508.

56 Y. M. Shanbhag, M. M. Shanbhag, S. J. Malode, S. Dhanalakshmi, K. Mondal and N. P. Shetti, *Biosensors*, 2022, **12**, 552.

57 L. Kong, Y. Liu, L. Dong, L. Zhang, L. Qiao, W. Wang and H. You, *Dalton Trans.*, 2020, **49**, 1947–1954.

58 M. Yaseen, M. Humayun, A. Khan, M. Idrees, N. Shah and S. Bibi, *Molecules*, 2022, **27**, 5343.

59 M. Yaseen, S. Farooq, A. Khan, N. Shah, L. A. Shah, S. Bibi, I. U. Khan and S. Ahmad, *J. Chin. Chem. Soc.*, 2022, **69**, 1637–1653.

60 P. Kumar, E. Vahidzadeh, U. K. Thakur, P. Kar, K. M. Alam, A. Goswami, N. Mahdi, K. Cui, G. M. Bernard and V. K. Michaelis, *J. Am. Chem. Soc.*, 2019, **141**, 5415–5436.

61 M. Humayun, M. He, W. Feng, C. Jin, Z. Yao, Y. Wang, W. Pi, S. Ali, A. Khan and M. Wang, *Sol. Energy*, 2021, **215**, 121–130.

62 S. Ali, M. Humayun, W. Pi, Y. Yuan, M. Wang, A. Khan, P. Yue, L. Shu, Z. Zheng and Q. Fu, *J. Hazard. Mater.*, 2020, **397**, 122708.

63 H.-B. Fang, Y. Luo, Y.-Z. Zheng, W. Ma and X. Tao, *Ind. Eng. Chem. Res.*, 2016, **55**, 4506–4514.

64 M. Kashif, S. Muhammad, A. Ali, K. Ali, S. Khan, S. Zahoor and M. Hamza, *J. Xi'an Shiyou Univ.*, 2023, **19**, 521–544.

65 Z. Chen, T. Ma, Z. Li, W. Zhu and L. Li, *J. Mater. Sci. Technol.*, 2024, **179**, 198–207.

66 G. Panthi and M. Park, *Int. J. Mol. Sci.*, 2023, **24**, 15021.

67 M. Benedet, G. A. Rizzi, A. Gasparotto, N. Gauquelin, A. Orekhov, J. Verbeeck, C. Maccato and D. Barreca, *Appl. Surf. Sci.*, 2023, **618**, 156652.

68 K. Vignesh, S. Kang, B. S. Kwak and M. Kang, *Sep. Purif. Technol.*, 2015, **147**, 257–265.

69 J. Wang, Y. Xia, H. Zhao, G. Wang, L. Xiang, J. Xu and S. Komarneni, *Appl. Catal., B*, 2017, **206**, 406–416.

70 M. Wu, Y. Gong, T. Nie, J. Zhang, R. Wang, H. Wang and B. He, *J. Mater. Chem. A*, 2019, **7**, 5324–5332.